

Figure 6.12: The Rall model with static current injected a distance  $x$  along the equivalent cable while the soma is clamped at its resting potential. The schematic at left shows the recording set up. The potential at the site of the current injection and the current entering the soma are measured. The central diagram is the equivalent circuit for this case, and the corresponding formulas for the somatic current and dendritic voltage are given at the right.  $R_{soma}$  is the membrane resistance of the soma, and  $R_3$  and  $R_4$  are the resistances given in equations 6.26 and 6.27.

$R_\lambda \sinh(x/\lambda) \cosh((L-x)/\lambda) / \cosh(L/\lambda)$ . When  $L$  and  $x$  are both much larger than  $\lambda$ , this approaches the limiting value  $R_\lambda$ . The current attenuation is defined as the ratio of the somatic to electrode currents and is given by

$$\frac{I_{soma}}{I_e} = \frac{R_4}{R_3 + R_4} = \frac{\cosh((L-x)/\lambda)}{\cosh(L/\lambda)}. \quad (6.28)$$

The inward current attenuation (plotted in figure 6.11) for the recording configuration of figure 6.12 is identical to the outward voltage attenuation for figure 6.10 given by equation 6.25. Equality of the voltage attenuation measured in one direction and the current attenuation measured in the opposite direction is a general feature of linear cable theory.

## The Morphoelectrotonic Transform

The membrane potential for a neuron of complex morphology is obviously much more difficult to compute than the simple cases we have considered. Fortunately, efficient numerical schemes (discussed later in this chapter) exist for generating solutions for complex cable structures. However, even when the solution is known, it is still difficult to visualize the effects of a complex morphology on the potential. Zador, Agmon-Snir, and Segev (1995; see also Tsai et al., 1994) devised a scheme for depicting the attenuation and delay of the membrane potential for complex morphologies. The voltage attenuation, as plotted in figure 6.11, is not an appropriate quantity to represent geometrically because it is not additive. Consider three points along a cable satisfying  $x_1 > x_2 > x_3$ . The attenuation between  $x_1$  and  $x_3$  is the product of the attenuation from  $x_1$  to  $x_2$  and from  $x_2$  to  $x_3$ ,  $v(x_1)/v(x_3) = (v(x_1)/v(x_2))(v(x_2)/v(x_3))$ . An additive quantity can be obtained by taking the logarithm of the attenuation, due to the identity  $\ln(v(x_1)/v(x_3)) = \ln(v(x_1)/v(x_2)) + \ln(v(x_2)/v(x_3))$ . The morphoelectrotonic transform is a diagram of a neuron in which the distance between

*morphoelectrotonic transform*

any two points is determined by the logarithm of the ratio of the membrane potentials at these two locations, not by the actual size of the neuron.

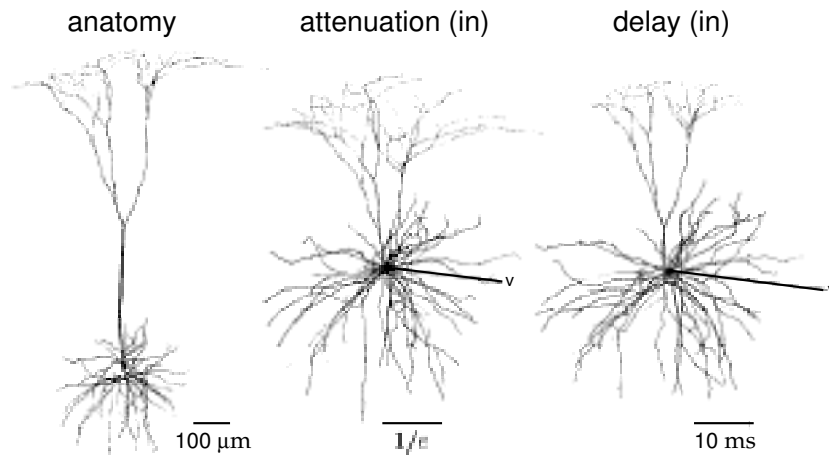


Figure 6.13: The morphoelectrotonic transform of a cortical neuron. The left panel is a normal drawing of the neuron. The central panel is a diagram in which the distance between any point and the soma is proportional to the logarithm of the steady-state attenuation between the soma and that point for static current injected at the terminals of the dendrites. The scale bar denotes the distance corresponding to an attenuation of  $\exp(-1)$ . In the right panel, the distance from the soma to a given point is proportional to the inward delay, which is the centroid of the soma potential minus the centroid at the periphery when a pulse of current is injected peripherally. The arrows in the diagrams indicate that the reference potential in these cases is the somatic potential. (Adapted from Zador et al, 1995.)

Another morphoelectrotonic transform can be used to indicate the amount of delay in the voltage waveform produced by a transient input current. The morphoelectrotonic transform uses a different definition of delay than that used in Figure 6.8B. The delay between any two points is defined as the difference between the centroid, or center of 'gravity', of the voltage response at these points. Specifically, the centroid at point  $x$  is defined as  $\int dt tv(x, t) / \int dt v(x, t)$ . Like the log-attenuation, the delay between any two points on a neuron is represented in the morphoelectrotonic transform as a distance.

Morphoelectrotonic transforms of a pyramidal cell from layer 5 of cat visual cortex are shown in figures 6.13 and 6.14. The left panel of figure 6.13 is a normal drawing of the neuron being studied, the middle panel shows the steady-state attenuation, and the right panel shows the delay. The transformed diagrams correspond to current being injected peripherally, with somatic potentials being compared to dendritic potentials. These figures indicate that, for potentials generated in the periphery, the apical and basal dendrites are much more uniform than the morphology would

suggest.

The small neuron diagram at the upper left of figure 6.14 shows attenuation for the reverse situation from figure 6.13, when DC current is injected into the soma and dendritic potentials are compared with the somatic potential. Note how much smaller this diagram is than the one in the central panel of figure 6.13. This illustrates the general feature mentioned previously that potentials are attenuated much less in the outward than in the inward direction. This is because the thin dendrites provide less of a current sink for potentials arising from the soma than the soma provides for potentials coming from the dendrites.

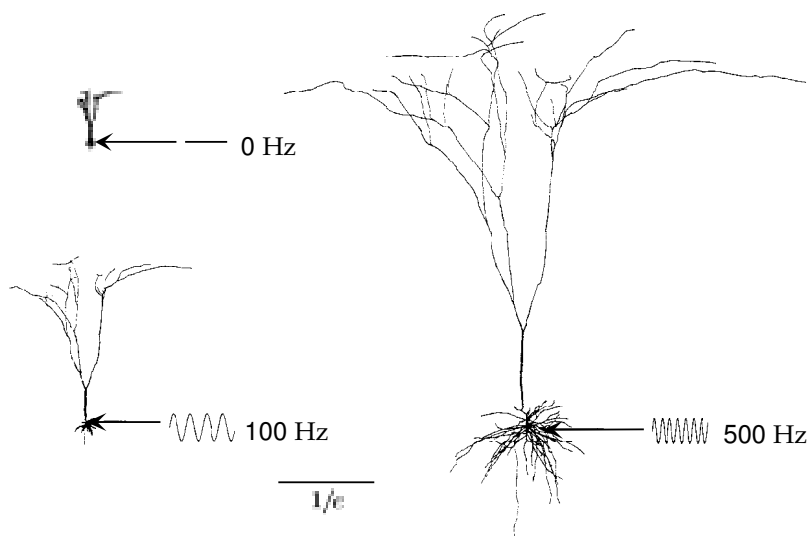


Figure 6.14: Morphoelectrotonic transforms of the same neuron as in figure 6.13 but showing the outward log-attenuation for DC and oscillating input currents. Distances in these diagrams are proportional to the logarithm of the amplitude of the voltage oscillations at a given point divided by the amplitude of the oscillations at the soma when a sinusoidal current is injected into the soma. The upper left panel corresponds to DC current injection, the lower left panel to sinusoidal current injection at a frequency of 100 Hz, and the right panel to an injection frequency of 500 Hz. The scale bar denotes the distance corresponding to an attenuation of  $\exp(-1)$ . (Adapted from Zador et al, 1995.)

The capacitance of neuronal cables causes the voltage attenuation for time-dependent current injection to increase as a function of frequency. Figure 6.14 compares the attenuation of dendritic potentials relative to the somatic potential when DC or sinusoidal current of two different frequencies is injected into the soma. Clearly, attenuation increases dramatically as a function of frequency. Thus, a neuron that appears electrotonically compact for static or low frequency current injection may be not compact when higher frequencies are considered. For example, action potential

waveforms, that correspond to frequencies around 500 Hz, are much more severely attenuated within neurons than slower varying potentials.

## 6.4 Multi-Compartment Models

The cable equation can only be solved analytically in relatively simple cases. When the complexities of real membrane conductances are included, the membrane potential must be computed numerically. This is done by splitting the neuron being modeled into separate regions or compartments and approximating the continuous membrane potential  $V(x, t)$  by a discrete set of values representing the potentials within the different compartments. This assumes that each compartment is small enough so that there is negligible variation of the membrane potential across it. The precision of such a multi-compartmental description depends on the number of compartments used and on their size relative to the length constants that characterize their electrotonic compactness. Figure 6.15 shows a schematic diagram of a cortical pyramidal neuron, along with a series of compartmental approximations of its structure. The number of compartments used can range from thousands, in some models, to one, for the description at the extreme right of figure 6.15.

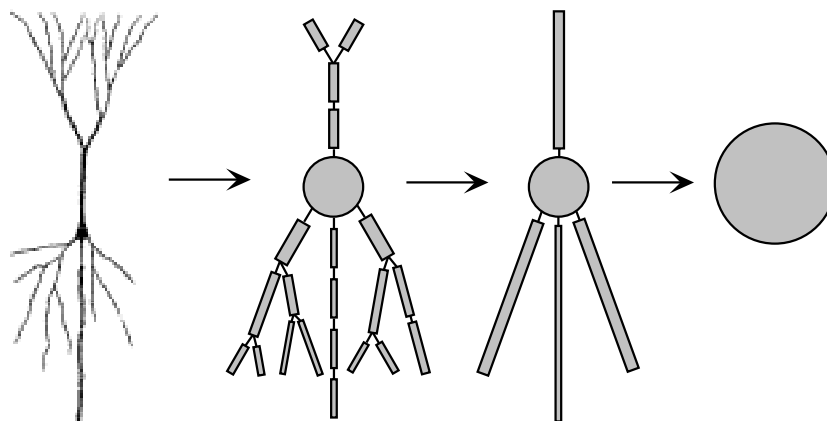


Figure 6.15: A sequence of approximations of the structure of a neuron. The neuron is represented by a variable number of discrete compartments each representing a region that is described by a single membrane potential. The connectors between compartments represent resistive couplings. The simplest description is the single-compartment model furthest to the right. (Neuron diagram from Haberly, 1990.)

In a multi-compartment model, each compartment has its own membrane potential  $V_\mu$  (where  $\mu$  labels compartments), and its own gating variables

that determine the membrane current for compartment  $\mu$ ,  $i_m^\mu$ . Each membrane potential  $V_\mu$  satisfies an equation similar to 6.1 except that the compartments couple to their neighbors in the multi-compartment structure (figure 6.16). For a non-branching cable, each compartment is coupled to two neighbors, and the equations for the membrane potentials of the compartments are

$$c_m \frac{dV_\mu}{dt} = -i_m^\mu + \frac{I_e^\mu}{A_\mu} + g_{\mu,\mu+1}(V_{\mu+1} - V_\mu) + g_{\mu,\mu-1}(V_{\mu-1} - V_\mu). \quad (6.29)$$

Here  $I_e^\mu$  is the total electrode current flowing into compartment  $\mu$ , and  $A_\mu$  is its surface area. Compartments at the ends of a cable have only one neighbor and thus only a single term replacing the last two terms in equation 6.29. For a compartment where a cable branches in two, there are three such terms corresponding to coupling of the branching node to the first compartment in each of the daughter branches.

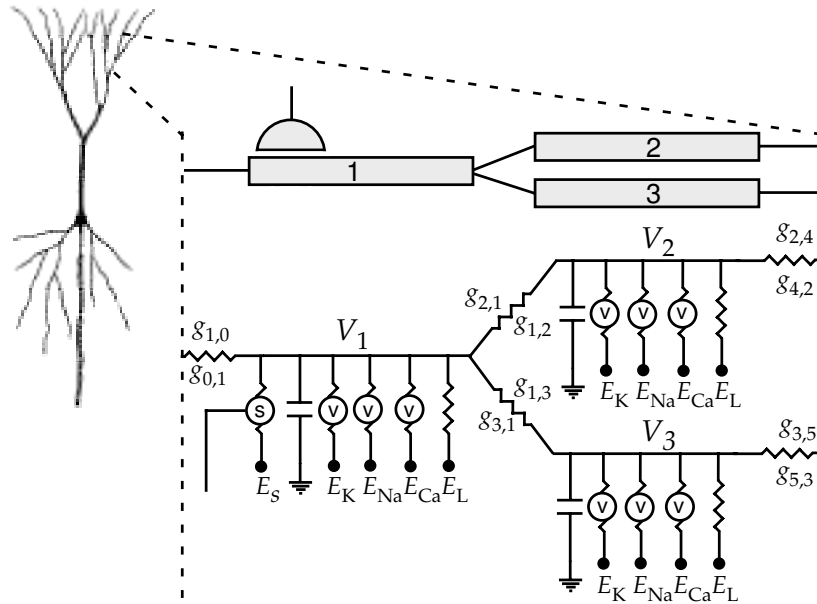


Figure 6.16: A multi-compartment model of a neuron. The expanded region shows three compartments at a branch point where a single cable splits into two. Each compartment has membrane and synaptic conductances, as indicated by the equivalent electrical circuit, and the compartments are coupled together by resistors. Although a single resistor symbol is drawn, note that  $g_{\mu,\mu'}$  is not necessarily equal to  $g_{\mu',\mu}$ .

The constant  $g_{\mu,\mu'}$  that determines the resistive coupling from neighboring compartment  $\mu'$  to compartment  $\mu$  is determined by computing the current that flows from one compartment to its neighbor due to Ohm's law. For simplicity, we begin by computing the coupling between two compartments that have the same length  $L$  and radius  $a$ . Using the results of

chapter 5, the resistance between two such compartments, measured from their centers, is the intracellular resistivity,  $r_L$  times the distance between the compartment centers divided by the cross-sectional area,  $r_L L / \pi a^2$ . The total current flowing from compartment  $\mu + 1$  to compartment  $\mu$  is then  $\pi a^2 (V_{\mu+1} - V_\mu) / r_L L$ . Equation 6.29 for the potential within a compartment  $\mu$  refers to currents per unit area of membrane. Thus, we must divide the total current from compartment  $\mu'$  by the surface area of compartment  $\mu$ ,  $2\pi a L$ . Thus, we find that  $g_{\mu,\mu'} = a / (2r_L L^2)$ .

The value of  $g_{\mu,\mu'}$  is given by a more complex expression if the two neighboring compartments have different lengths or radii. This can occur when a tapering cable is approximated by a sequence of cylindrical compartments, or at a branch point where a single compartment connects with two other compartments as in figure 6.16. In either case, suppose that compartment  $\mu$  has length  $L_\mu$  and radius  $a_\mu$  and compartment  $\mu'$  has length  $L_{\mu'}$  and radius  $a_{\mu'}$ . The resistance between these two compartments is the sum of the two resistances from the middle of each compartment to the junction between them,  $r_L L_\mu / (2\pi a_\mu^2) + r_L L_{\mu'} / (2\pi a_{\mu'}^2)$ . To compute  $g_{\mu,\mu'}$  we invert this expression and divide the result by the total surface area of compartment  $\mu$ ,  $2\pi a_\mu L_\mu$ , which gives

$$g_{\mu,\mu'} = \frac{a_\mu a_{\mu'}^2}{r_L L_\mu (L_\mu a_{\mu'}^2 + L_{\mu'} a_\mu^2)}. \quad (6.30)$$

Equations 6.29 for all of the compartments of a model determine the membrane potential throughout the neuron with a spatial resolution given by the compartment size. An efficient method for integrating the coupled multi-compartment equations is discussed in appendix B. Using this scheme, models can be integrated numerically with excellent efficiency, even those involving large numbers of compartments. Such integration schemes are built into neuron simulation software packages such as Neuron and Genesis.

## Action Potential Propagation Along an Unmyelinated Axon

As an example of multi-compartment modeling, we simulate the propagation of an action potential along an unmyelinated axon. In this model, each compartment has the same membrane conductances as the single-compartment Hodgkin-Huxley model discussed in chapter 5. The different compartments are joined together in a single non-branching cable representing a length of axon. Figure 6.17 shows an action potential propagating along an axon modeled in this way. The action potential extends over more than 1 mm of axon and it travels about 2 mm in 5 ms for a speed of 0.4 m/s.

Although action potentials typically move along axons in a direction outward from the soma (called orthodromic propagation), the basic process

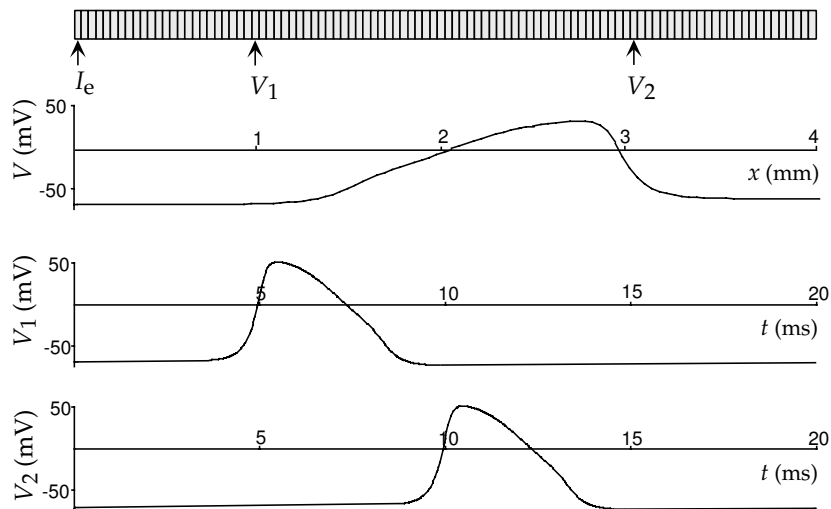


Figure 6.17: Propagation of an action potential along a multi-compartment model axon. The upper panel shows the multi-compartment representation of the axon with 100 compartments. The axon segment shown is 4 mm long and has a radius of  $1 \mu\text{m}$ . An electrode current sufficient to initiate action potentials is injected at the point marked  $I_e$ . The panel beneath this shows the membrane potential as a function of position along the axon, at  $t = 9.75 \text{ ms}$ . The spatial position in this panel is aligned with the axon depicted above it. The action potential is moving to the right. The bottom two panels show the membrane potential as a function of time at the two locations denoted by the arrows and symbols  $V_1$  and  $V_2$  in the upper panel.

*orthodromic;  
antidromic  
propagation*

of action potential propagation does not favor one direction over the other. Propagation in the reverse direction, called antidromic propagation, is possible under certain stimulation conditions. For example, if an axon is stimulated in the middle of its length, action potentials will propagate in both directions away from the point of stimulation. Once an action potential starts moving along an axon, it does not generate a second action potential moving in the opposite direction because of refractory effects. The region in front of a moving action potential is ready to generate a spike as soon as enough current moves longitudinally down the axon from the region currently spiking to charge the next region up to spiking threshold. However,  $\text{Na}^+$  conductances in the region just behind the moving action potential are still partially inactivated, so this region cannot generate another spike until after a recovery period. By the time the trailing region has recovered, the action potential has moved too far away to generate a second spike.

Refractoriness following spiking has a number of other consequences for action potential propagation. Two action potentials moving in opposite directions that collide annihilate each other because they cannot pass through each other's trailing refractory regions. Refractoriness also keeps

action potentials from reflecting off the ends of axon cables, which avoids the impedance matching needed to prevent reflection from the ends of ordinary electrical cables.

The propagation velocity for an action potential along an unmyelinated axon is proportional to the ratio of the electrotonic length constant to the membrane time constant,  $\lambda/\tau_m = (a/(c_m^2 r_L r_m))^{1/2}$ . This is proportional to the square root of the axon radius. The square-root dependence of the propagation speed on the axon radius means that thick axons are required to achieve high action potential propagation speeds, and the squid giant axon is an extreme example. Action potential propagation can also be sped up by covering the axon with an insulating myelin wrapping, as we discuss next.

### Propagation Along a Myelinated Axon

Many axons in vertebrates are covered with an insulating sheath of myelin, except at gaps, called the nodes of Ranvier, where there is a high density of fast voltage-dependent  $\text{Na}^+$  channels and other ion channels (see figure 6.18A). The myelin sheath consists of many layers of (glial cell) membrane wrapped around the axon. This gives the myelinated region of the axon a very high membrane resistance and a small membrane capacitance. This results in what is called saltatory propagation, in which membrane potential depolarization is transferred passively down the myelin-covered sections of the axon, and action potentials are actively regenerated at the nodes of Ranvier. The cell membrane at the nodes of Ranvier has a high density of fast  $\text{Na}^+$  channels. Figure 6.18A shows an equivalent circuit for a multi-compartment model of a myelinated axon.

*saltatory  
propagation*

We can compute the capacitance of a myelin-covered axon by treating the myelin sheath as an extremely thick cell membrane. Consider the geometry shown in the cross-sectional diagram of figure 6.18B. The myelin sheath extends from the radius  $a_1$  of the axon core to the outer radius  $a_2$ . For calculational purposes, we can think of the myelin sheath as being made of a series of thin concentric cylindrical shells. The capacitances of these shells combine in series to make up the full capacitance of the myelinated axon. If a single layer of cell membrane has thickness  $d_m$  and capacitance per unit area  $c_m$ , the capacitance of a cylinder of membrane of radius  $a$ , thickness  $\Delta a$ , and length  $L$  is  $c_m 2\pi d_m L a / \Delta a$ . According to the rule for capacitors in series, the inverse of the total capacitance is obtained by adding the inverses of the individual capacitances. The capacitance of a myelinated cylinder of length  $L$  and the dimensions in figure 6.18B is then obtained by taking the limit  $\Delta a \rightarrow 0$  and integrating,

$$\frac{1}{C_m} = \frac{1}{c_m 2\pi d_m L} \int_{a_1}^{a_2} \frac{da}{a} = \frac{\ln(a_2/a_1)}{c_m 2\pi d_m L}. \quad (6.31)$$

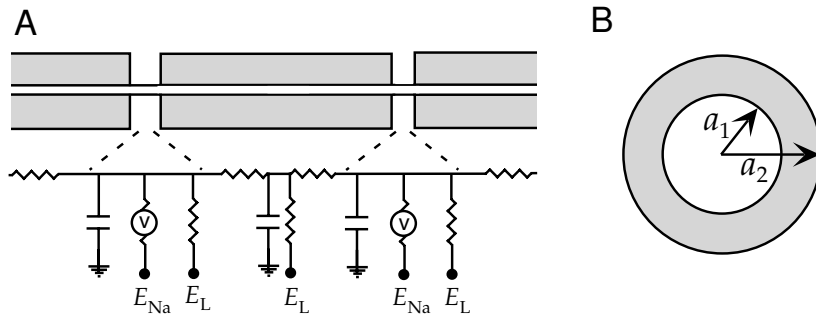


Figure 6.18: A myelinated axon. A) The equivalent circuit for a multi-compartment representation of a myelinated axon. The myelinated segments are represented by a membrane capacitance, a longitudinal resistance, and a leakage conductance. The nodes of Ranvier also contain a voltage-dependent  $\text{Na}^+$  conductance. B) A cross-section of a myelinated axon consisting of a central axon core of radius  $a_1$  and a myelin sheath making the outside radius  $a_2$ .

A re-evaluation of the derivation of the linear cable equation earlier in this chapter indicates that the equation describing the membrane potential along the myelinated sections of an axon, in the limit of infinite resistance for the myelinated membrane and with  $i_e = 0$ , is

$$\frac{C_m}{L} \frac{\partial v}{\partial t} = \frac{\pi a_1^2}{r_L} \frac{\partial^2 v}{\partial x^2}. \quad (6.32)$$

This is equivalent to the diffusion equation,  $\partial v / \partial t = D \partial^2 v / \partial x^2$  with diffusion constant  $D = \pi a_1^2 L / (C_m r_L) = a_1^2 \ln(a_2 / a_1) / (2 c_m r_L d_m)$ . It is interesting to compute the inner core radius,  $a_1$ , that maximizes this diffusion constant for a fixed outer radius  $a_2$ . Setting the derivative of  $D$  with respect to  $a_1$  to zero gives the optimal inner radius  $a_1 = a_2 \exp(-1/2)$  or  $a_1 \approx 0.6 a_2$ . An inner core fraction of 0.6 is typical for myelinated axons. This indicates that, for a given outer radius, the thickness of myelin maximizes the diffusion constant along the myelinated axon segment.

At the optimal ratio of radii,  $D = a_2^2 / (4 e c_m r_L d_m)$ , which is proportional to the square of the axon radius. Because of the form of the diffusion equation it obeys with this value of  $D$ ,  $v$  can be written as a function of  $x/a_2$  and  $t$ . This scaling implies that the propagation velocity for a myelinated cable is proportional to  $a_2$ , that is, to the axon radius not its square root as in the case of an unmyelinated axon. Increasing the axon radius by a factor of four, for example, increases the propagation speed of an unmyelinated cable only by a factor of two, while it increases the speed for a myelinated cable fourfold.

## 6.5 Chapter Summary

We continued the discussion of neuron modeling that began in chapter 5 by considering models with more complete sets of conductances and techniques for incorporating neuronal morphology. We introduced A-type  $K^+$ , transient  $Ca^{2+}$ , and  $Ca^{2+}$ -dependent  $K^+$  conductances and noted their effect on neuronal activity. The cable equation and its linearized version were introduced to examine the effects of morphology on membrane potentials. Finally, multi-compartment models were presented and used to discuss propagation of action potentials along unmyelinated and myelinated axons.

## 6.6 Appendices

### A) Gating Functions for Conductance-Based Models

#### Connor-Stevens Model

The rate functions used for the gating variables  $n$ ,  $m$ , and  $h$  of the Connor-Stevens model, in units of  $1/\text{ms}$  with  $V$  in units of  $\text{mV}$ , are

$$\begin{aligned} \alpha_m &= \frac{0.38(V + 29.7)}{1 - \exp[-0.1(V + 29.7)]} & \beta_m &= 15.2 \exp[-0.0556(V + 54.7)] \\ \alpha_h &= 0.266 \exp[-0.05(V + 48)] & \beta_h &= 3.8 / (1 + \exp[-0.1(V + 18)]) \\ \alpha_n &= \frac{0.02(V + 45.7)}{1 - \exp[-.1(V + 45.7)]} & \beta_n &= 0.25 \exp[-0.0125(V + 55.7)]. \end{aligned} \quad (6.33)$$

The A-current is described directly in terms of the asymptotic values and  $\tau$  functions for its gating variables (with  $\tau_a$  and  $\tau_b$  in units of  $\text{ms}$  and  $V$  in units of  $\text{mV}$ ),

$$a_\infty = \left[ \frac{0.0761 \exp[0.0314(V + 94.22)]}{1 + \exp[0.0346(V + 1.17)]} \right]^{1/3} \quad (6.34)$$

$$\tau_a = 0.3632 + 1.158 / (1 + \exp[0.0497(V + 55.96)]) \quad (6.35)$$

$$b_\infty = \left[ \frac{1}{1 + \exp[0.0688(V + 53.3)]} \right]^4 \quad (6.36)$$

and

$$\tau_b = 1.24 + 2.678 / (1 + \exp[0.0624(V + 50)]) . \quad (6.37)$$

**Transient Ca<sup>2+</sup> Conductance**

The gating functions used for the variables  $M$  and  $H$  in the transient Ca<sup>2+</sup> conductance model we discussed, with  $V$  in units of mV and  $\tau_M$  and  $\tau_H$  in ms, are

$$M_\infty = \frac{1}{1 + \exp(-(V + 57)/6.2)} \quad (6.38)$$

$$H_\infty = \frac{1}{1 + \exp((V + 81)/4)} \quad (6.39)$$

$$\tau_M = 0.612 + (\exp(-(V + 132)/16.7) + \exp((V + 16.8)/18.2))^{-1} \quad (6.40)$$

and

$$\tau_H = \begin{cases} \exp((V + 467)/66.6) & \text{if } V < -80 \text{ mV} \\ 28 + \exp(-(V + 22)/10.5) & \text{if } V \geq -80 \text{ mV}. \end{cases} \quad (6.41)$$

**Ca<sup>2+</sup>-dependent K<sup>+</sup> Conductance**

The gating functions used for the Ca<sup>2+</sup>-dependent K<sup>+</sup> conductance we discussed, with  $V$  in units of mV and  $\tau_c$  in ms, are

$$c_\infty = \left( \frac{[\text{Ca}^{2+}]}{[\text{Ca}^{2+}] + 3\mu\text{M}} \right) \frac{1}{1 + \exp(-(V + 28.3)/12.6)} \quad (6.42)$$

and

$$\tau_c = 90.3 - \frac{75.1}{1 + \exp(-(V + 46)/22.7)}. \quad (6.43)$$

**B) Integrating Multi-Compartment Models**

Multi-compartmental models are defined by a coupled set of differential equations (equation 6.29), one for each compartment. There are also gating variables for each compartment, but these only involve the membrane potential (and possibly Ca<sup>2+</sup> concentration) within that compartment, and integrating their equations can be handled as in the single-compartment case using the approach discussed in appendix B of chapter 5. Integrating the membrane potentials for the different compartments is more complex because they are coupled to each other.

Equation 6.29 for the membrane potential within compartment  $\mu$  can be written in the form

$$\frac{dV_\mu}{dt} = A_\mu V_{\mu-1} + B_\mu V_\mu + C_\mu V_{\mu+1} + D_\mu \quad (6.44)$$

where

$$\begin{aligned} A_\mu &= c_m^{-1} g_{\mu, \mu-1}, & B_\mu &= -c_m^{-1} \left( \sum_i g_i^\mu + g_{\mu, \mu+1} + g_{\mu, \mu-1} \right), \\ C_\mu &= c_m^{-1} g_{\mu, \mu+1}, & \text{and } D_\mu &= c_m^{-1} \left( \sum_i g_i^\mu E_i + I_e^\mu / A_\mu \right). \end{aligned} \quad (6.45)$$

Note that the gating variables and other parameters have been absorbed into the values of  $A_\mu$ ,  $B_\mu$ ,  $C_\mu$ , and  $D_\mu$  in this equation. Equation 6.44, with  $\mu$  running over all of the compartments of the model, generates a set of coupled differential equations. Because of the coupling between compartments, we cannot use the method discussed in appendix A of chapter 5 to integrate these equations. Instead, we present another method that shares some of the positive features of that method.

Two of the most important features of an integration method are accuracy and stability. Accuracy refers to how closely numerical finite-difference methods reproduce the exact solution of a differential equation as a function of the integration step size  $\Delta t$ . Stability refers to what happens when  $\Delta t$  is chosen to be excessively large and the method starts to become inaccurate. A stable integration method will degrade smoothly as  $\Delta t$  is increased, producing results of steadily decreasing accuracy. An unstable method, on the other hand, will, at some point, display a sudden transition and generate wildly inaccurate results. Given the tendency of impatient modelers to push the limits on  $\Delta t$ , it is highly desirable to have a method that is stable.

Defining

$$V_\mu(t + \Delta t) = V_\mu(t) + \Delta V_\mu, \quad (6.46)$$

the finite difference form of equation 6.44 gives the update rule

$$\Delta V_\mu = (A_\mu V_{\mu-1}(t) + B_\mu V_\mu(t) + C_\mu V_{\mu+1}(t) + D_\mu) \Delta t \quad (6.47)$$

which is how  $\Delta V_\mu$  is computed using the so-called Euler method. This method is both inaccurate and unstable. The stability of the method can be improved dramatically by evaluating the membrane potentials on the right side of equation 6.47 not at time  $t$ , but at a later time  $t + z\Delta t$ , so that

$$\Delta V_\mu = (A_\mu V_{\mu-1}(t + z\Delta t) + B_\mu V_\mu(t + z\Delta t) + C_\mu V_{\mu+1}(t + z\Delta t) + D_\mu) \Delta t. \quad (6.48)$$

Two such methods are predominantly used, the reverse Euler method for which  $z = 1$  and the Crank-Nicholson method with  $z = 0.5$ . The reverse Euler method is the more stable of the two and the Crank-Nicholson is the more accurate. In either case,  $\Delta V_\mu$  is determined from equation 6.48. These methods are called implicit because equation 6.48 must be solved to determine  $\Delta V_\mu$ . To do this, we write  $V_\mu(t + z\Delta t) \approx V_\mu(t) + z\Delta V_\mu$  and likewise for  $V_{\mu\pm 1}$ . Substituting this into equation 6.48 gives

$$\Delta V_\mu = a_\mu \Delta V_{\mu-1} + b_\mu \Delta V_\mu + c_\mu \Delta V_{\mu+1} + d_\mu \quad (6.49)$$

where

$$\begin{aligned} a_\mu &= A_\mu z \Delta t, \quad b_\mu = B_\mu z \Delta t, \quad c_\mu = C_\mu z \Delta t, \quad \text{and} \\ d_\mu &= (D_\mu + A_\mu V_{\mu-1}(t) + B_\mu V_\mu(t) + C_\mu V_{\mu+1}(t)) \Delta t. \end{aligned} \quad (6.50)$$

Equation 6.49 for all  $\mu$  values provides a set of coupled linear equations for the quantities  $\Delta V_\mu$ . An efficient method exists for solving these equations (Hines 1984, Tuckwell 1988). We illustrate the method for a single, non-branching cable that begins with at compartment  $\mu = 1$ , so that  $a_1 = 0$ , and ends at compartment  $\mu = N$ , so  $c_N = 0$ . The method consists of solving equation 6.49 for  $\Delta V_\mu$  in terms of  $\Delta V_{\mu+1}$  sequentially starting at one end of the cable and proceeding to the other end. For example, if we start the procedure at compartment one,  $\Delta V_1$  can be expressed as

$$\Delta V_1 = \frac{c_1 \Delta V_2 + d_1}{1 - b_1}. \quad (6.51)$$

Substituting this into the equation 6.49 for  $\mu = 2$  gives

$$\Delta V_2 = b'_2 \Delta V_2 + c_2 \Delta V_3 + d'_2 \quad (6.52)$$

where  $b'_2 = b_2 + a_2 c_1 / (1 - b_1)$  and  $d'_2 = d_2 + a_2 d_1 / (1 - b_1)$ . We now repeat the procedure going down the cable. At each stage, we solve for  $\Delta V_{\mu-1}$  in terms of  $\Delta V_\mu$  finding

$$\Delta V_{\mu-1} = \frac{c_{\mu-1} \Delta V_\mu + d'_{\mu-1}}{1 - b'_{\mu-1}}. \quad (6.53)$$

where

$$b'_{\mu+1} = b_{\mu+1} + \frac{a_{\mu+1} c_\mu}{1 - b'_\mu} \quad (6.54)$$

and

$$d'_{\mu+1} = d_{\mu+1} + \frac{a_{\mu+1} d'_\mu}{1 - b'_\mu}. \quad (6.55)$$

Finally, when we get to the end of the cable we can solve for

$$\Delta V_N = \frac{d'_N}{1 - b'_N} \quad (6.56)$$

because  $c_N = 0$ .

The procedure for computing all the  $\Delta V_\mu$  is the following. Define  $b'_1 = b_1$  and  $d'_1 = d_1$  and iterate equations 6.54 and 6.55 down the length of the cable to define all the  $b'$  and  $d'$  parameters. Then, solve for  $\Delta V_N$  from equation 6.56 and iterate back up the cable solving for the  $\Delta V$ 's using 6.53. This process takes only  $2N$  steps.

We leave the extension of this method to the case of a branched cable as an exercise for the reader. The general procedure is similar to the one we presented for a non-branching cable. The equations are solved starting at the ends of the branches and moving in toward their branching node, then continuing on as for a non-branching cable, and finally reversing direction and completing the solution moving in the opposite direction along the cable and its branches.

## 6.7 Annotated Bibliography

Many of the references for chapter 5 apply to this chapter as well, including **Jack et al. (1975)**; **Tuckwell (1988)**; **Johnston & Wu (1995)**; **Koch & Segev (1998)**; **Koch (1998)**; **Hille (1992)**; **Mascagni & Sherman (1998)**. **Rall (1977)** describes cable theory, the equivalent cable model of dendritic trees, and the 3/2 law. **Marder & Calabrese, (1996)** review neuromodulation.

Two freely available modeling packages for detailed neural models are in wide use, *Neuron* (see Hines & Carnevale, 1997) and *Genesis* (see Bower & Beeman, 1998). These are available at <http://www.neuron.yale.edu> and <http://genesis.bbb.caltech.edu/GENESIS/genesis.html>.